Supporting Information

Aqueous Proton Battery Stably Operates in Mild Electrolyte and Low-Temperature Condition

*Tianjiang Sun [a], Qingshun Nian [b], Haihui Du [a], Shibing Zheng [a], Dong Han [a], Zhanliang Tao [a]**

[a]Key Laboratory of Advanced Energy Materials Chemistry (Ministry of Education), Renewable Energy Conversion and Storage Center, College of Chemistry, Nankai University, Haihe Laboratory of Sustainable Chemical Transformations
Tianjin 300071, P. R. China

[b]Hefei National Laboratory for Physical Science at the Microscale, CAS Key Laboratory of Materials for Energy Conversion, Department of Materials Science and Engineering, University of Science and Technology of China Hefei, Anhui 230026, China

E-mail: taozhl@nankai.edu.cn

The calculation details about the utilization rate of electrolyte

In this work, the active material is Mn^{2+} in electrolyte. For example, 50 μL (73.06 mg) 3.5 M $Mn(ClO_4)_2$ electrolyte is added in coin cell. Theoretically, this electrolyte can provide a capacity of 9.3819 mAh. The calculated process can be summarized as follow:

1. The mole of Mn^{2+}: 3.5 mol L^{-1} × 50 μL × 10^{-6} = 1.75×10^{-4} mol

2. The mole of formed MnO_2 in theory: 1.75×10^{-4} mol

3. The theoretical capacity of Mn^{2+}/MnO_2: $C = \frac{96500 \times n}{3.6 \times Mr_{MnO_2}}$ = 96500×2÷(3.6×87)=616.22 mAh g^{-1}

4. The max capacity which can be provided by electrolyte: 616.22 mAh g^{-1} × 1.75×10^{-4} mol × 87 g mol^{-1}=9.3819 mAh

5. The PANI//CF battery obtains a capacity of 0.122 mAh at 2 C. It implies that the utilization rate of electrolyte only has 1.3% (0.122÷9.3819×100%).

PANI is selected to verify the feasibility of the cathode (based on conversion reaction of Mn^{2+}/MnO_2) in full battery. Considering practical application value, suitable anodes with higher theoretical capacity should be developed and applied to match this cathode.

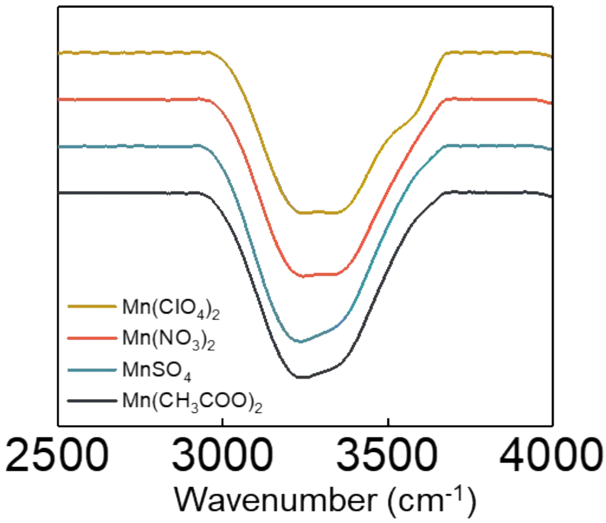

Figure S1. The stretching vibration of H_2O.

Following the order of $Mn(CH_3COO)_2$-$MnSO_4$-$Mn(NO_3)_2$-$Mn(ClO_4)_2$, the peak at low wavenumber, corresponding to strong hydrogen bond, gradually decrease. The peak at high wavenumber, corresponding to weak hydrogen bond, gradually increase.

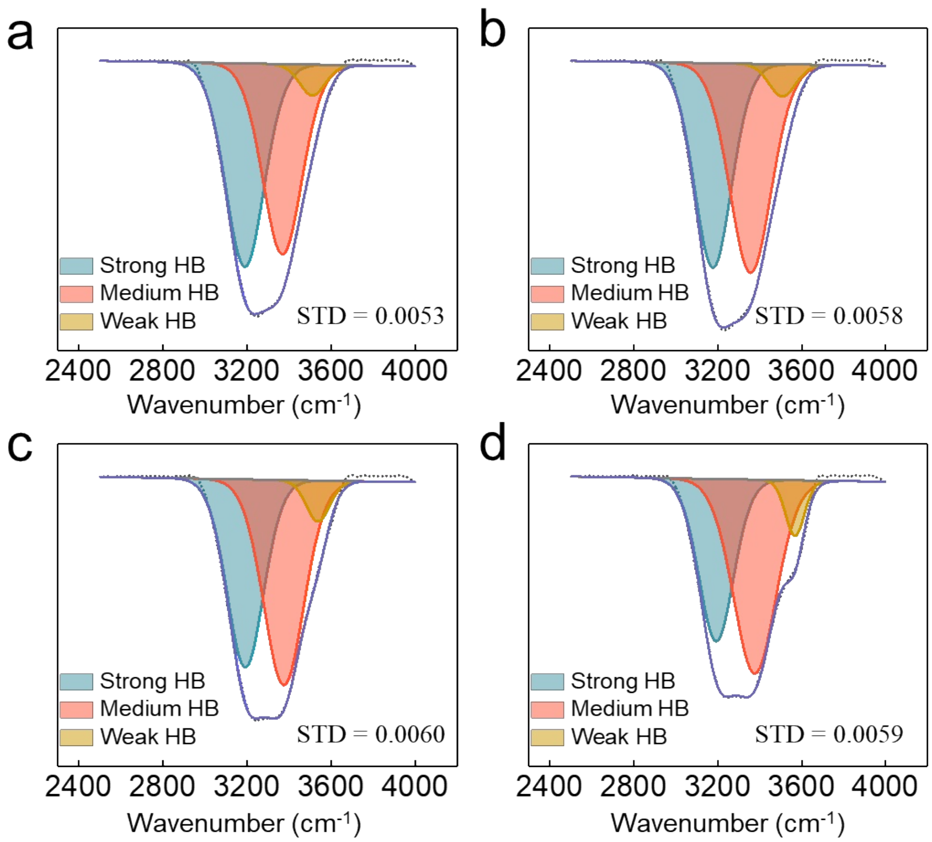

Figure S2. The fitted O-H stretching vibration of H_2O in a) 1 M $Mn(CH_3COO)_2$; b) 1 M $MnSO_4$; c) 1 M $Mn(NO_3)_2$; d) 1 M $Mn(ClO_4)_2$.

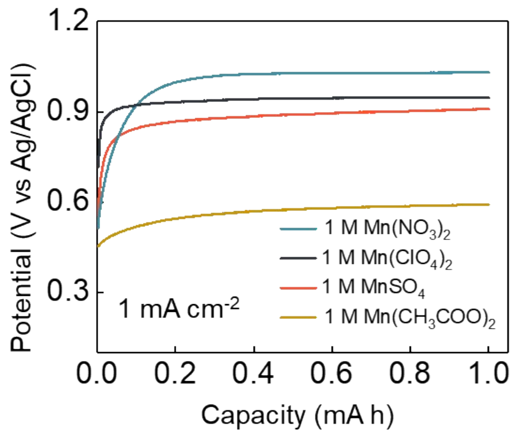

Figure S3. The charge curves of CF electrodes in different electrolytes.

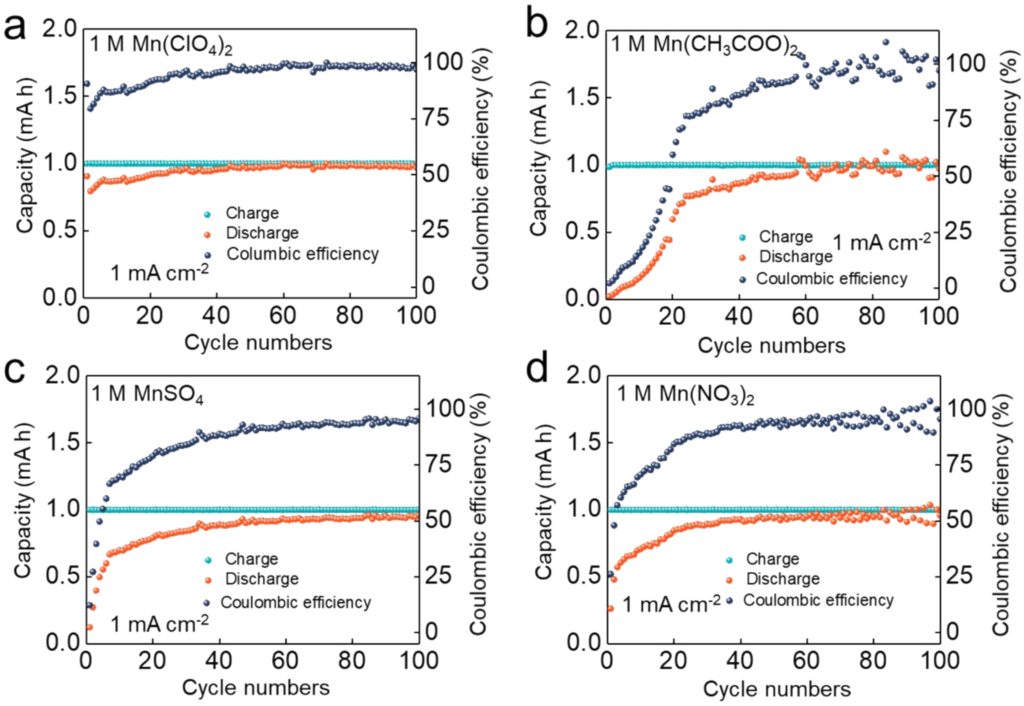

Figure S4. The cycling stability of CF electrode in a) 1 M $Mn(ClO_4)_2$; b) 1 M $Mn(CH_3COO)_2$; c) 1 M $MnSO_4$; d) 1 M $Mn(NO_3)_2$.

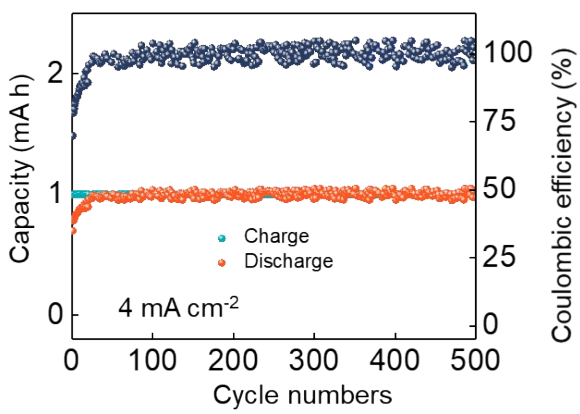

Figure S5. The cycling stability of CF electrode at 4 mA cm^{-2} in 1 M $Mn(ClO_4)_2$.

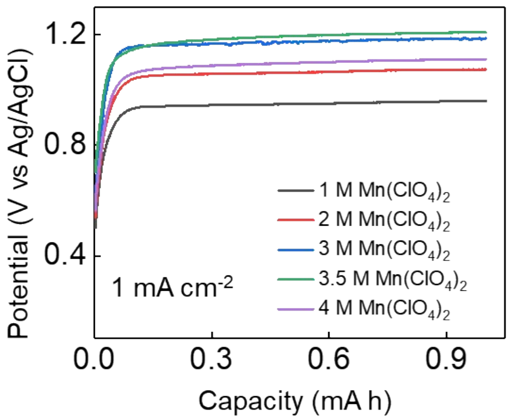

Figure S6. The charge curves of CF electrodes in different concentrations $Mn(ClO_4)_2$ electrolyte.

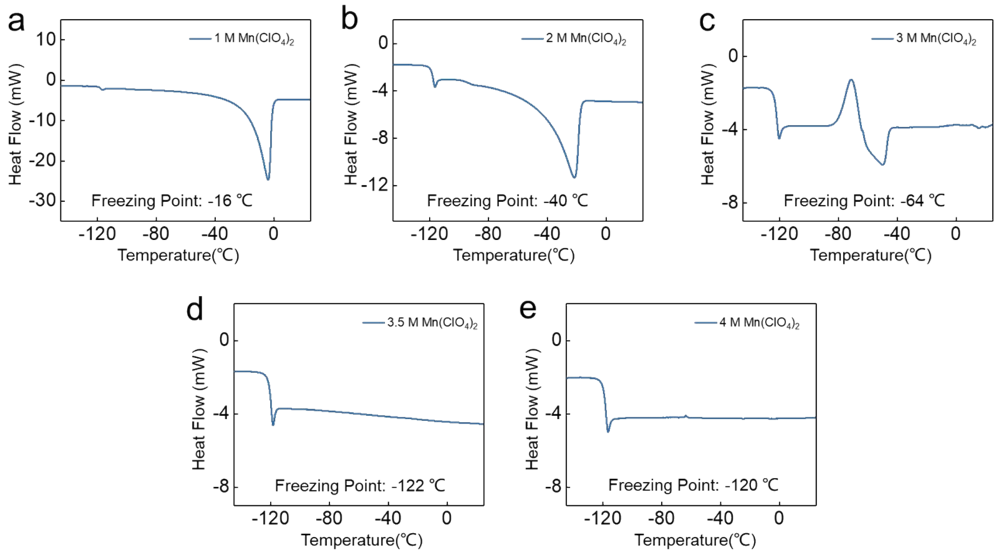

Figure S7. The freezing point of a) 1 M $Mn(ClO_4)_2$; b) 2 M $Mn(ClO_4)_2$; c) 3 M $Mn(ClO_4)_2$; d) 3.5 M $Mn(ClO_4)_2$. e) 4 M $Mn(ClO_4)_2$.

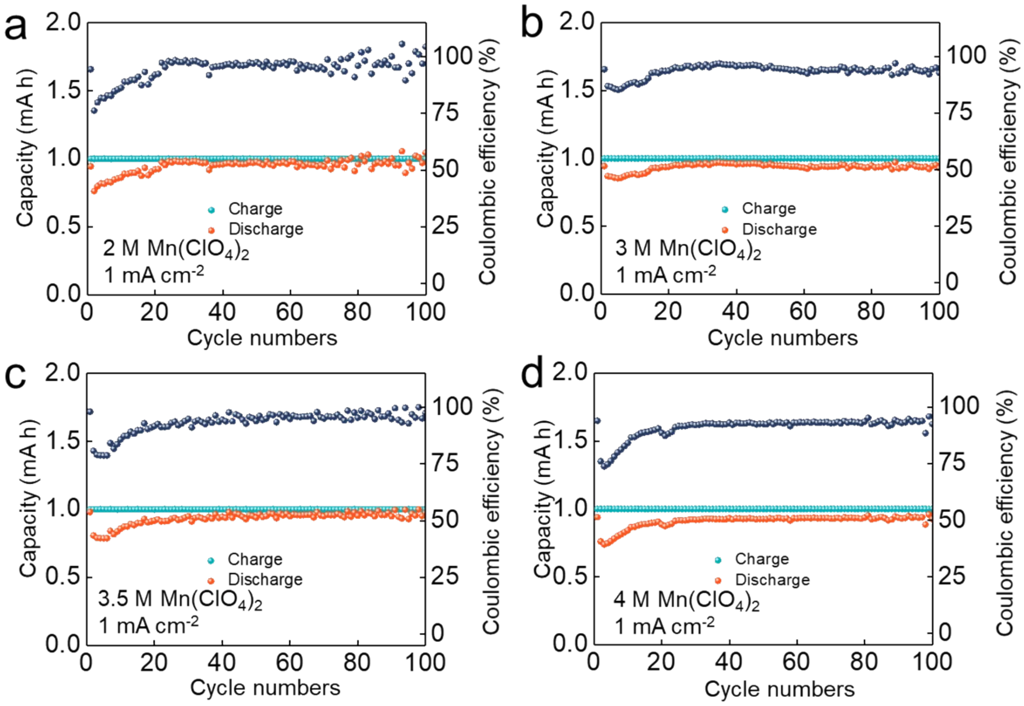

Figure S8. The cycling stability of CF electrode in a) 2 M $Mn(ClO_4)_2$; b) 3 M $Mn(ClO_4)_2$; c) 3.5 M $Mn(ClO_4)_2$; d) 4 M $Mn(ClO_4)_2$.

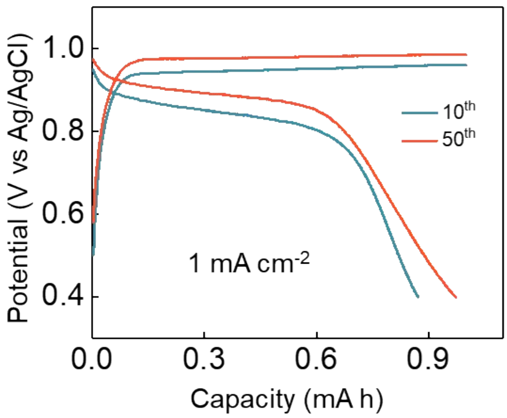

Figure S9. The charge-discharge curves of CF electrode in 3.5 M $Mn(ClO_4)_2$ electrolyte.

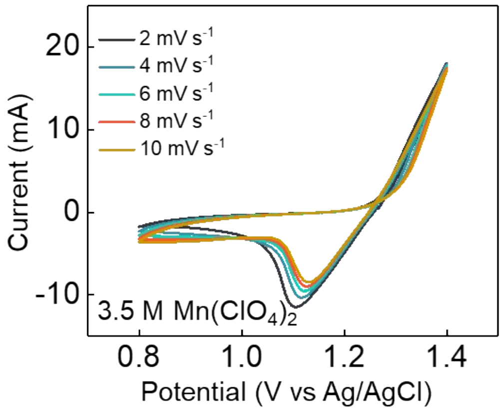

Figure S10. The different scan-rate CV curves of CF electrode in 3.5 M $Mn(ClO_4)_2$ electrolyte.

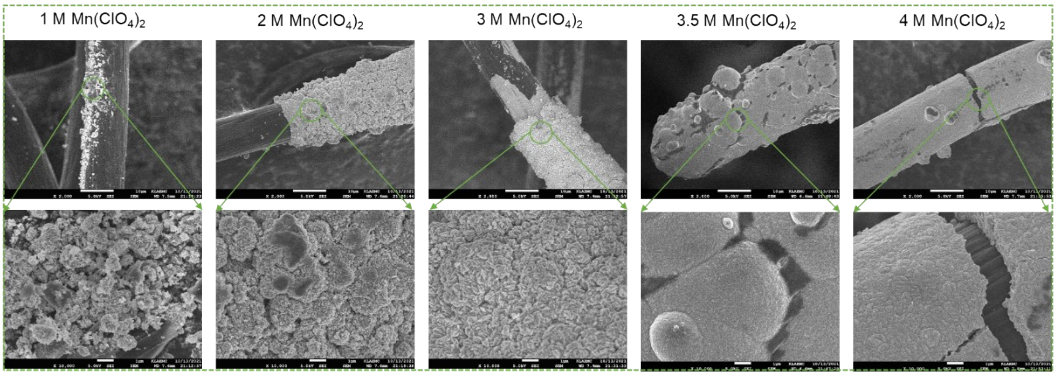

Figure S11. The deposition morphology of MnO_2 on the surface of CF electrode in different concentrations $Mn(ClO_4)_2$ electrolytes.

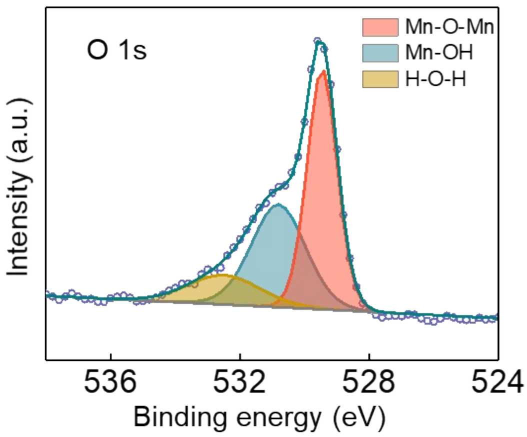

Figure S12. The XPS spectrum of O 1s.

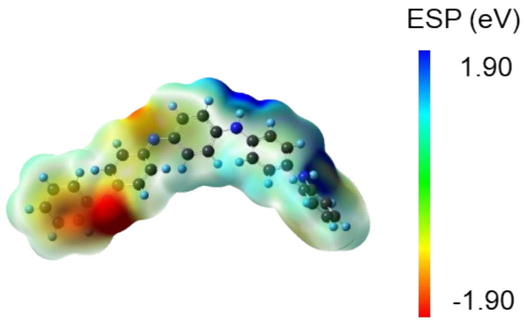

Figure S13. The ESP of PANI.

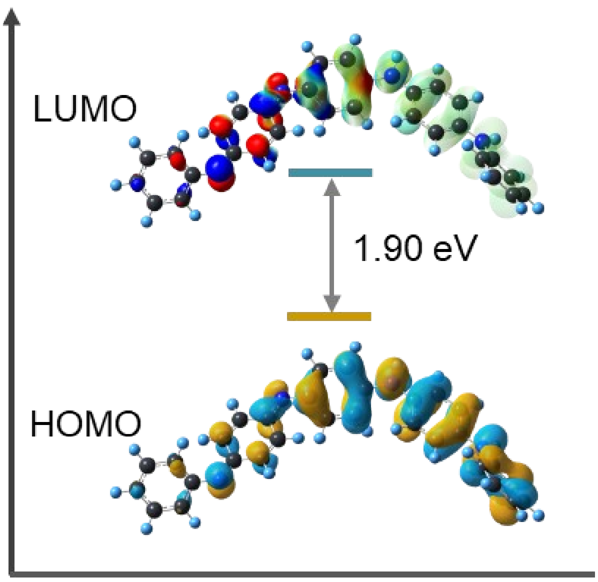

Figure S14. The LUMO-HOMO energy gap of PANI.

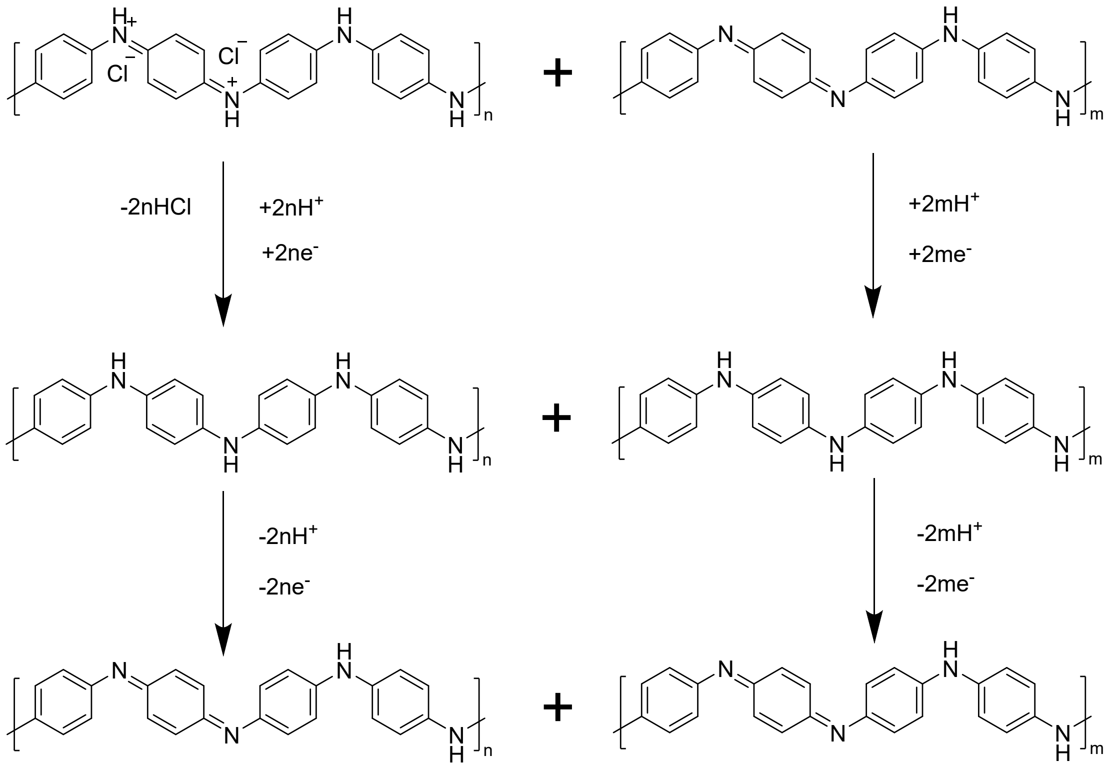

Figure S15. The possible reaction mechanism of PANI.

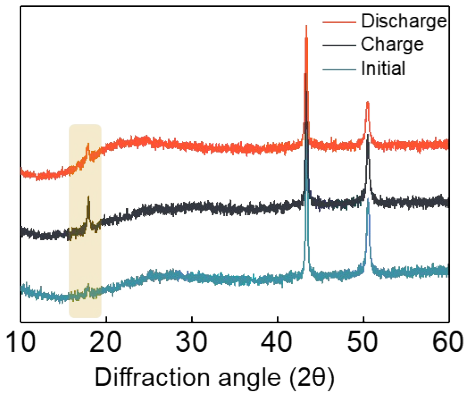

Figure S16. The ex-site XRD patterns of PANI electrodes.

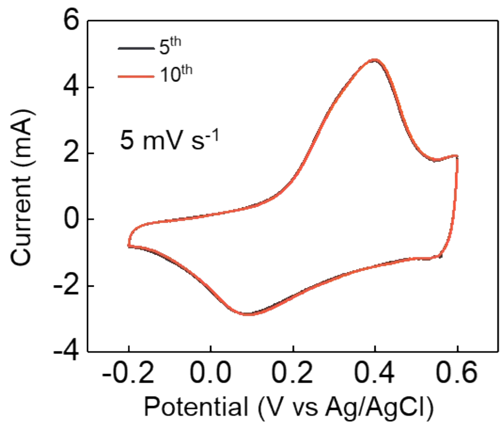

Figure S17. The CV curves of PANI electrode.

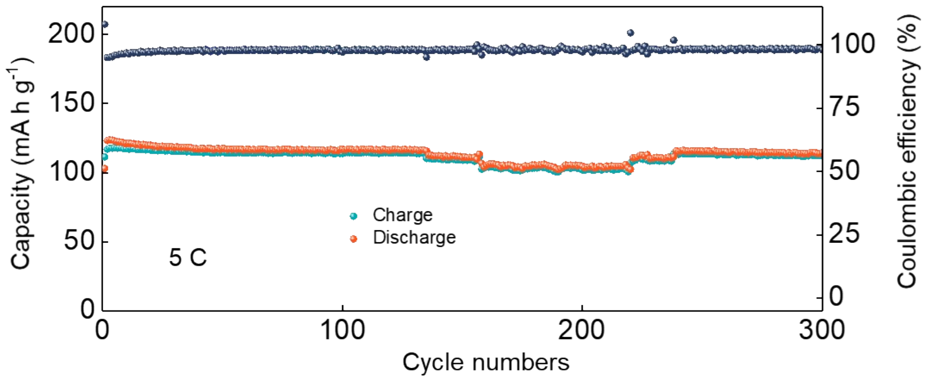

Figure S18. The cycling stability of PANI electrode.

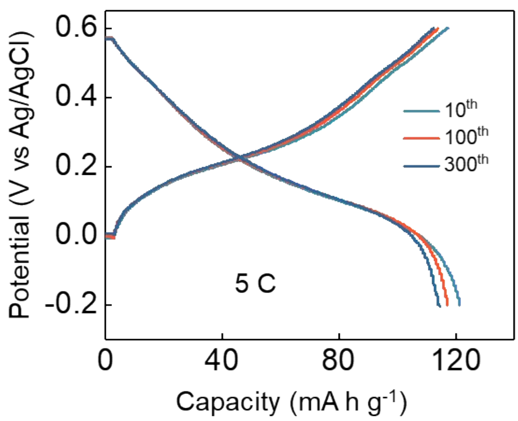

Figure S19. The charge-discharge curves of PANI electrode.

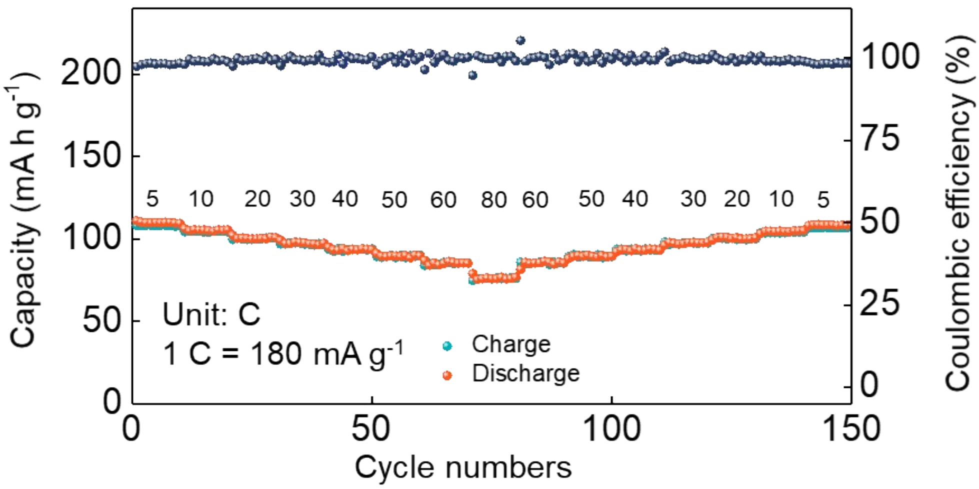

Figure S20. The rate capability of PANI electrode.

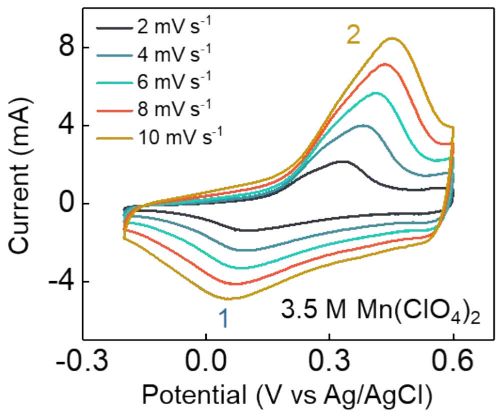

Figure S21. The different scan-rate CV curves of PANI electrode.

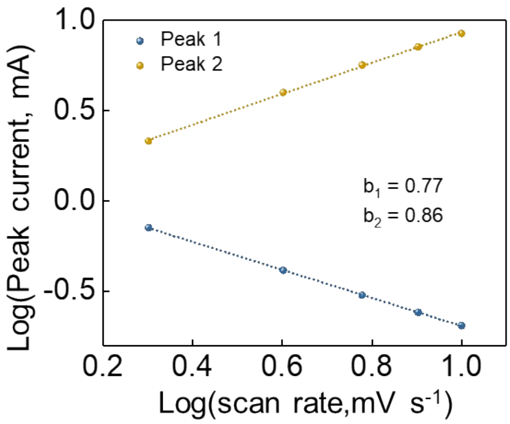

Figure S22. The calculated *b* values of PANI electrode.

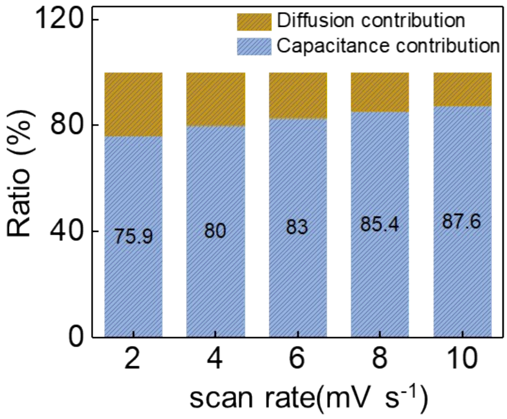

Figure S23. The calculated capacitance contribution ratio of PANI electrode.

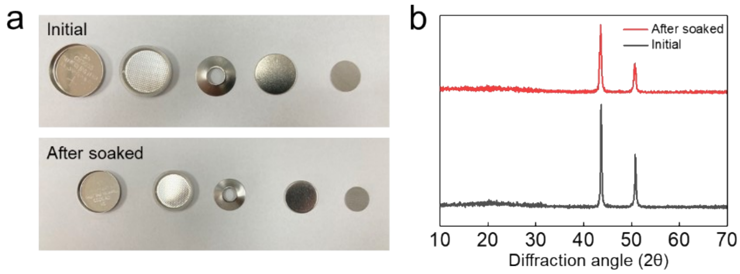

Figure S24. a) the optical images of cell shells; b) the XRD patterns of stainless steel current collector (SS).

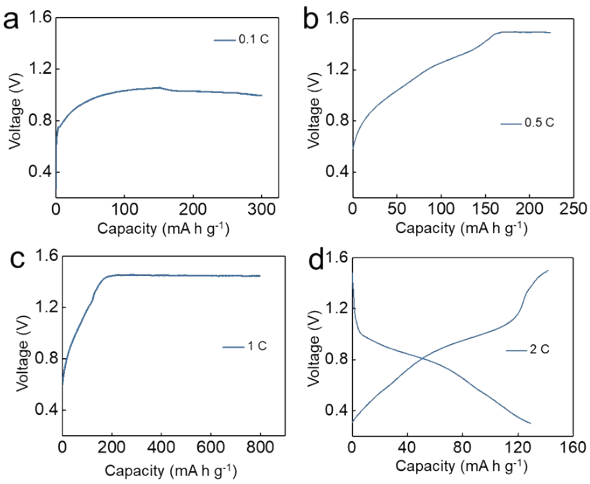

Figure S25. The charging curves of PANI//CF battery at a) 0.1 C; b) 0.5 C; c) 1C; d) the charge-discharge curve of PANI//CF battery at 2 C.

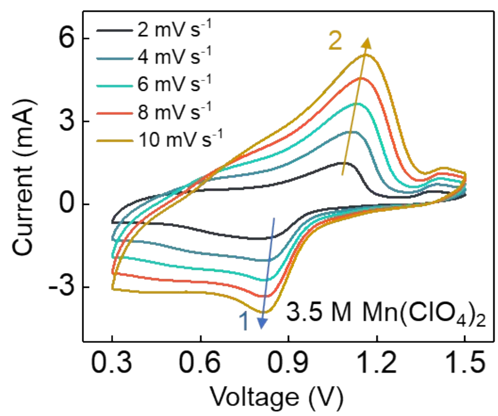

Figure S26. The different scan-rate CV curves of PANI//CF battery.

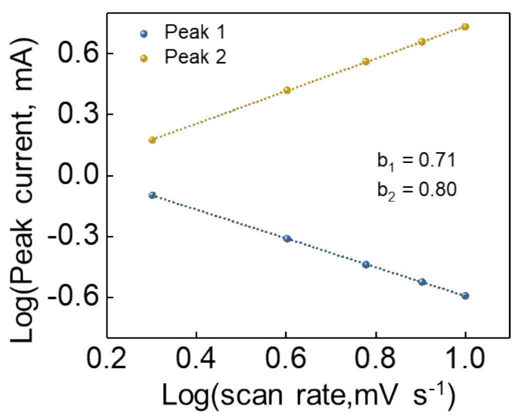

Figure S27. The calculated *b* values of PANI//CF battery.

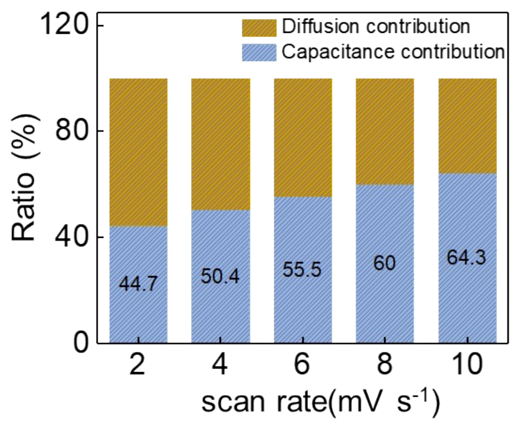

Figure S28. The calculated capacitance contribution ratio of PANI//CF battery.

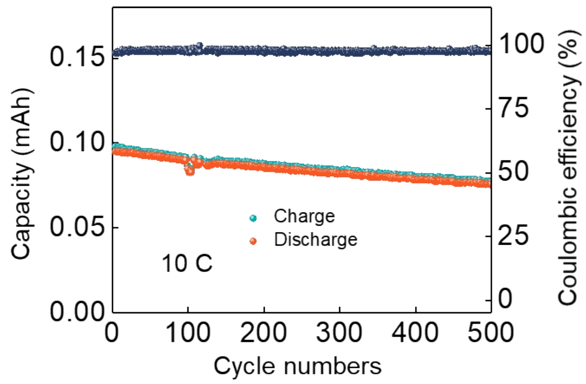

Figure S29. The cycling performance of CF//PANI battery.

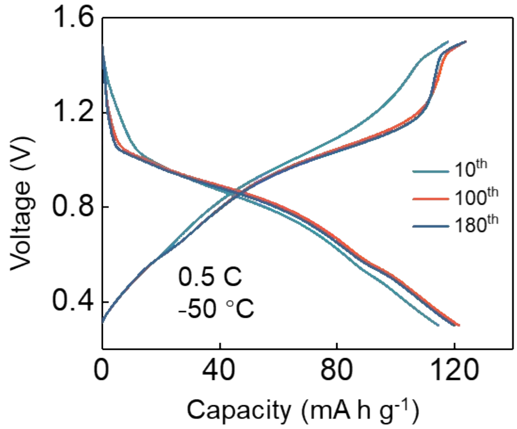

Figure S30. The charge-discharge curves of PANI//CF battery at -50 °C.

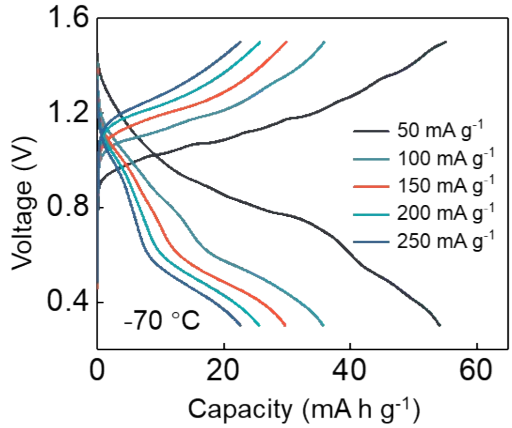

Figure S31. The rate capability of PANI//CF battery at -70 °C.

Table S1. The comparison of this work and reported works.

Cathode	Anode	Electrolyte	Discharge capacity /current density	Ref.
MnO_2@GF	PTO	2 M H_2SO_4+ 2 M $MnSO_4$	208 mA h g^{-1}/0.16 mA cm^{-2}	[1]
MnO_2@GF	MoO_3	2 M H_2SO_4+ 2 M $MnSO_4$	209.6 mA h g^{-1}/1 A g^{-1}	[2]
MnO_2@CF	ALO	2 M HBF_4+ 2 M $Mn(BF_4)_2$	145.5 mA h g^{-1}/1 A g^{-1}	[3]
MnO_2@CF	Zn	0.1 M H_2SO_4+ 2 M $MnSO_4$ +1 M $ZnSO_4$	\	[4]
MnO_2@CF	Pb	0.5 M H_2SO_4+ 1 M $MnSO_4$	\	[5]
MnO_2@CF	**PANI**	**3.5 M $Mn(ClO_4)_2$**	**130 mA h g^{-1}/ 0.7 A g^{-1}**	**This work**

Table S2. The ex-situ DES of PANI electrodes at different states.

Element \ State		initial	charge	discharge
C	Atomic Fraction (%)	75.34	48.04	56.35
N		24.66	51.96	43.17
Mn		0.00	0.00	0.18

Reference

[1]. Guo Z.; Huang J.; Dong X.; Xia Y.; Yan L.; Wang Z. Wang Y., An Organic/Inorganic Electrode-Based Hydronium-Ion Battery. *Nat. Commun.*, **2020**, *11*(1), 959.

[2]. Yan L.; Huang J.; Guo Z.; Dong X.; Wang Z. Wang Y., Solid-State Proton Battery Operated at Ultralow Temperature. *ACS Energy Lett.*, **2020**, *5*(2), 685-691.

[3]. Sun T.; Du H.; Zheng S.; Shi J. Tao Z., High Power and Energy Density Aqueous Proton Battery Operated at −90 °C. *Adv. Funct. Mater.*, **2021**, *31*(16), 2010127.

[4]. Chao D.; Zhou W.; Ye C.; Zhang Q.; Chen Y.; Gu L.; Davey K. Qiao S. Z., An Electrolytic Zn-Mno2 Battery for High-Voltage and Scalable Energy Storage. *Angew. Chem., Int. Ed.*, **2019**, *58*(23), 7823-7828.

[5]. Huang J.; Yan L.; Bin D.; Dong X.; Wang Y. Xia Y., An Aqueous Manganese–Lead Battery for Large-Scale Energy Storage. *J. Mater. Chem. A*, **2020**, *8*(12), 5959-5967.